. .

Supplementary Information for

Ultrafast space-time optical merons in momentum-energy space

Murat Yessenov,[1,2,*] Ahmed H. Dorrah,[2] Cheng Guo,[3,4] Layton A. Hall,[1] Joon-Suh Park,[2] Justin Free,[5] Eric G. Johnson,[5] Federico Capasso,[2] Shanhui Fan,[3,4] and Ayman F. Abouraddy[1,†]

[1]*CREOL, The College of Optics & Photonics, University of Central Florida, Orlando, Florida 32816, USA*

[2]*Harvard John A. Paulson School of Engineering and Applied Sciences, Harvard University, Cambridge, MA 02138, USA*

[3]*E. L. Ginzton Laboratory, Stanford University, Stanford, CA, USA*

[4]*Department of Electrical Engineering, Stanford University, Stanford, CA, USA*

[5]*Micro-Photonics Laboratory, Center for Optical Materials Science and Engineering Technologies (COMSET), Holcombe Department of Electrical and Computer Engineering, Clemson University, 215 Riggs Hall, Clemson, SC 29634, USA*

[*] yessenov@ucf.edu

[†] raddy@creol.ucf.edu

CONTENTS

I. Theory of space-time (ST) merons in momentum-energy space S3

A. Jones vector representation of meron polarization texture S4

II. Synthesis of ST merons S5

A. Spectral Analysis S5

1. Spatially resolving the spectrum via chirped volume Bragg gratings (CBGs) S5

2. Characterization of the spatially separated spectrum S6

B. Spectral transformation S7

1. Methodology S7

2. Experimental implementation S9

C. Coordinate transformation S10

1. Methodology S10

2. Design of the phase profiles S11

3. Fabrication of diffractive phase plates for the coordinate transformation S11

D. Metasurface for implementing a meron spin-texture S13

1. Metasurface design S13

2. Metasurface fabrication S16

3. Metasurface characterization S18

III. Characterization of ST merons S19

A. Spatio-temporal spectral intensity S19

B. Spectral Stokes polarimetry S21

C. Extracting Skyrmion number from the measurements of Stokes parameters S21

D. Spatiotemporally resolved Stokes polarimetry S22

References S23

I. THEORY OF SPACE-TIME (ST) MERONS IN MOMENTUM-ENERGY SPACE

Skyrmions and merons are topological configurations of a three-component unit vector field $\boldsymbol{n}(\boldsymbol{r})$ on a 2-sphere parameter space with coordinates $\boldsymbol{r}=(x,y,z)$. These configurations are distinguished by a nonzero topological number (Skyrmion number):

$$N=\frac{1}{4\pi}\int \boldsymbol{n}\cdot\left(\frac{\partial \boldsymbol{n}}{\partial x}\times\frac{\partial \boldsymbol{n}}{\partial y}\right)\mathrm{d}x\mathrm{d}y, \tag{1}$$

which quantifies the number of times $\boldsymbol{n}(\boldsymbol{r})$ wraps around the unit sphere. Skyrmions and anti-skyrmions, characterized by $N=\pm 1$, indicate that $\boldsymbol{n}(\boldsymbol{r})$ covers the entire unit sphere. An example is a configuration where $\boldsymbol{n}=\hat{z}$ at the disk's center and $\boldsymbol{n}=-\hat{z}$ at its perimeter. In contrast, merons and antimerons, characterized by $N=\pm\frac{1}{2}$, indicate that $\boldsymbol{n}(\boldsymbol{r})$ covers only a hemisphere (Fig. 1A of the Main text). For instance, $\boldsymbol{n}=\hat{z}$ at the disk's center, and $\boldsymbol{n}\perp\hat{z}$ at its perimeter. Hence, merons are also known as half-skyrmions.

This paper examines the polarization texture of photons in momentum-energy space, represented by the normalized Stokes parameters:

$$\boldsymbol{n}=(n_x,n_y,n_z)=\left(\frac{S_1}{S_0},\frac{S_2}{S_0},\frac{S_3}{S_0}\right). \tag{2}$$

All $\boldsymbol{n}$'s form the Poincaré sphere. The base space is a curved surface in (k_x,k_y,ω) space (Fig. 1B of the Main text). We present an explicit construction of the meron polarization texture:

$$\boldsymbol{n}(k_r,\phi_k)=\frac{1}{\sqrt{k_r^2+\kappa^2}}\left(k_r\cos(\phi_k+\gamma),k_r\sin(\phi_k+\gamma),\kappa\right). \tag{3}$$

Here we adopt the polar coordinates:

$$k_r=\sqrt{k_x^2+k_y^2},\quad \phi_k=\arg(k_x+ik_y). \tag{4}$$

The parameter κ specifies the meron's radius in wavevector space, while the helicity parameter $\gamma\in(-\pi,\pi]$ determines the meron type—Néel type for $\gamma=0,\pi$ and Bloch type for $\gamma=\pi/2,-\pi/2$ (Fig. S1)

t is worth emphasizing that throughout this paper we manipulate the polarization (also known as spin) textures of optical fields in both spatiotemporal and momentum-energy space. In the paraxial narrow-band regime that we focus on here the light polarization is described by the Stokes parameters (S_1,S_2,S_3) and they can encode more information than merely spin angular momentum components in the propagation directions, which is characterized by S_3 only. This is in contrast to optical realizations of skyrmion in plasmonic systems, where skyrmionic textures are imprinted onto the electric field profiles [1] or time-averaged spin vectors [2, 3].

A. Jones vector representation of meron polarization texture

We presented above an explicit construction of the meron polarization texture. Here we provide an equivalent representation using Jones vectors, which specify the electromagnetic fields more explicitly.

We begin with a two-band Hamiltonian:

$$\hat{H}(k_x,k_y;\kappa,\gamma)=\left(-k_x\cos\gamma+k_y\sin\gamma\right)\hat{\tau}x+\left(-k_x\sin\gamma-k_y\cos\gamma\right)\hat{\tau}y-\kappa\hat{\tau}_z. \tag{5}$$

Here, $\hat{\tau}_x,\hat{\tau}_y,\hat{\tau}_z$ represent Pauli matrices. The bases $(1,0)^T$, $(0,1)^T$, $\frac{1}{\sqrt{2}}(1,1)^T$, and $\frac{1}{\sqrt{2}}(1,-1)^T$ correspond to right circular, left circular, x, and y polarizations, respectively.

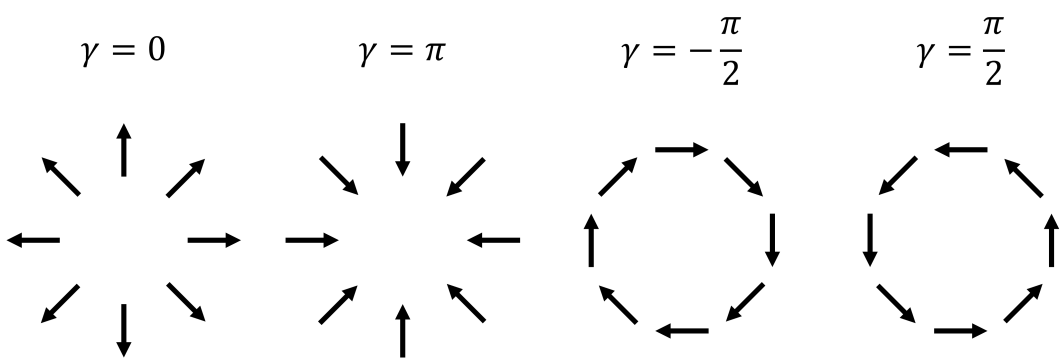

FIG. S1. Illustration of the helicity parameter γ

We choose the lower eigenstate of $\hat{H}$ to define our Jones vector. We define

$$\theta(k_r,\phi_k)=\pi-\arccos\frac{\kappa}{\sqrt{k_r^2+\kappa^2}},\quad \theta\in[\pi/2,\pi); \tag{6}$$

$$\varphi(k_r,\phi_k)=\phi_k+\gamma-\pi,\qquad \varphi\in[-\pi,\pi). \tag{7}$$

Then we obtain:

$$\boldsymbol{E}(k_r,\phi_k)\equiv\begin{pmatrix}E_{rcp}(k_r,\phi_k)\\E_{lcp}(k_r,\phi_k)\end{pmatrix}=E_0(k_r,\phi_k)\begin{pmatrix}\sin\frac{\theta}{2}\\-e^{i\varphi}\cos\frac{\theta}{2}\end{pmatrix}, \tag{8}$$

where $E_0(k_r,\phi_k)$ is a scalar function that specifies the complex amplitude envelope.

II. SYNTHESIS OF ST MERONS

A. Spectral Analysis

1. *Spatially resolving the spectrum via chirped volume Bragg gratings (CBGs)*

The first step to synthesizing an ST meron is to spatially resolve the spectral content of the incident pulsed optical field, which we achieve using a chirped volume Bragg grating (CBG) [4] whose grating period varies longitudinally. Consequently, when an optical pulse is incident onto the CBG, each wavelength reflects from a different depth within it where the Bragg condition is met. Therefore, when the field is incident normally onto the CBG, a group delay is introduced between the different temporal frequencies (that is, *temporal chirp*), thus yielding a stretched pulse [5, 6]. This property of CBGs is widely used for pulse stretching and compression in high-power chirped pulse amplification (CPA) systems in light of the high damage threshold, high efficiency,

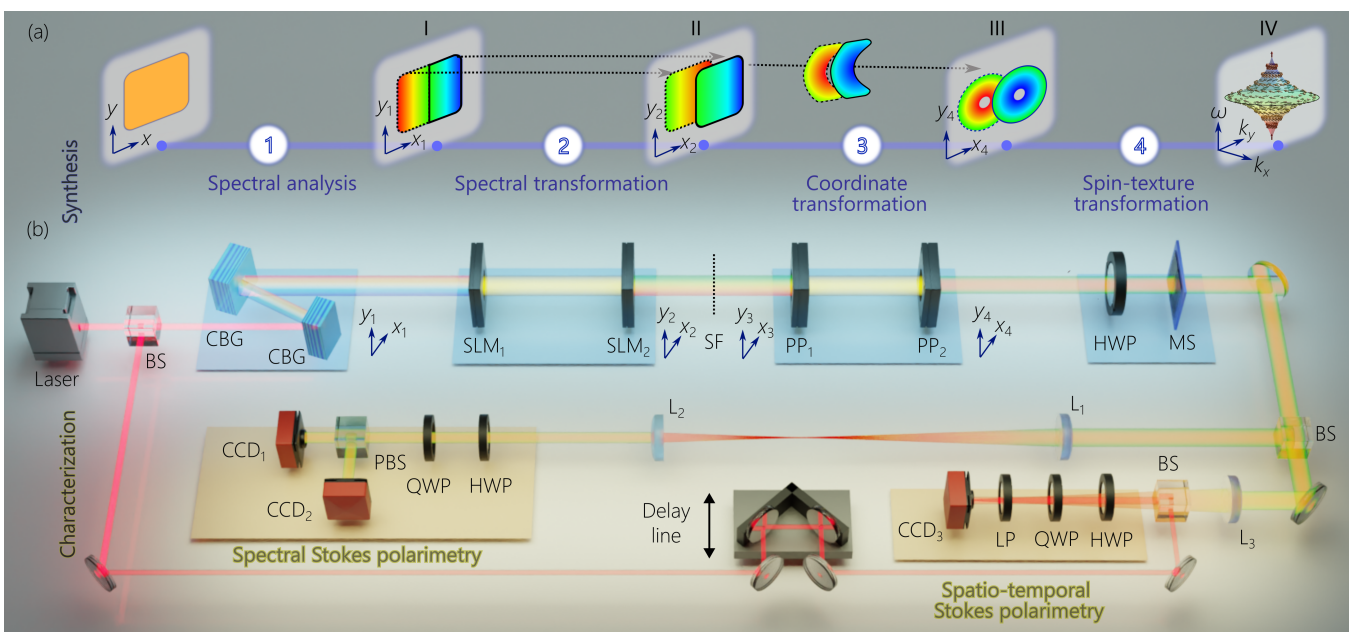

FIG. S2. (a) Layout of the field manipulation throughout each stage of the ST meron synthesis. (b) Experimental setup for the synthesis and characterization of the ST meron. Here, CBG: chirped volume Bragg grating, SLM: spatial light modulator, PP: phase plate, MS: metasurface, HWP: half-wave plate; QWP: quarter-wave plate, LP: linear polarizer, BS: beam splitter, PBS: polarizing beam splitter, L: spherical lens, SF: spatial filter, CCD: charged-coupled device camera.

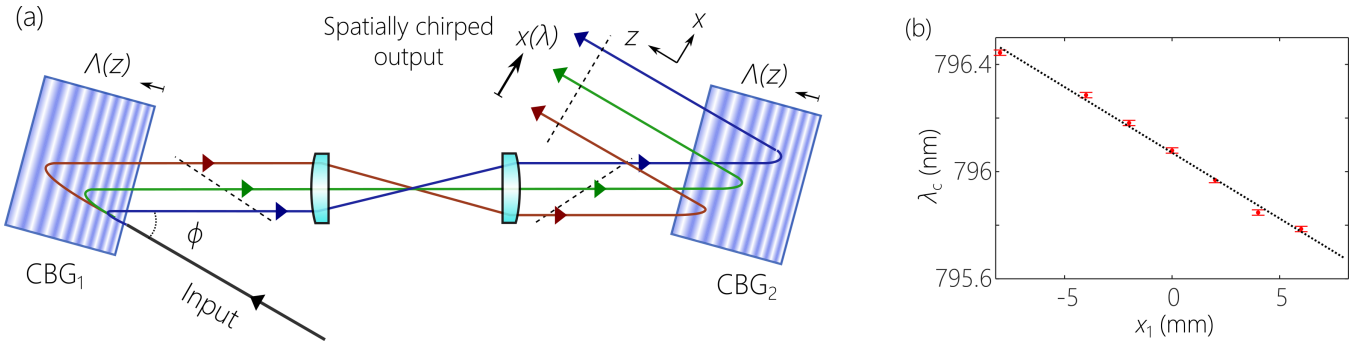

FIG. S3. (a) Spatially resolving the spectrum via a pair of CBGs (CBG_1 and CBG_2) at oblique incidence. First, CBG_1 introduces both temporal and spatial chirps into the input pulse. The sign of the spatial chirp is then reversed via a $4f$ system. When the field interacts with CBG_2 (which is identical to CBG_1), the temporal chirp is canceled while the spatial chirp is doubled. After CBG_2, the optical field is spatially resolved along the horizontal axis x_1 with no temporal chirp. (b) Measurements of the spatial chirp $\lambda_c(x_1)$ at the output of the system in (a). Adopted from ref. [11]

and potential for introducing extremely large temporal chirps [7]. A less-known property of CBGs is their ability to introduce a *spatial chirp* (resolving the spectrum spatially) along with a temporal chirp when the pulse is incident obliquely on a conventional CBG [8], or incident normally on a so-called rotated CBG (r-CBG) in which the Bragg structure is rotated with respect to the input facet [9]. For our purpose, it is crucial to remove the temporal chirp while retaining the spatial chirp. This is achieved by directing the field emerging from the CBG to an identical CBG placed in a reversed geometry with respect to the first [6, 10]. We show this procedure in Fig. S3(a) unfolded for clarity.

2. *Characterization of the spatially separated spectrum*

We confirm the spatial chirp across the spatially resolved spectrum by scanning a single-mode fiber (Thorlabs 780HP) across the wavefront emerging from the double-pass CBG system. The fiber is connected to an optical spectrum analyzer (OSA, Advantest AQ6317B), and the measured spectrum is plotted in Fig. S3(b). The measured spectrum has a bandwidth $\Delta\lambda \approx 0.8$ nm centered at $\lambda_c \approx 796$ nm spread spatially over 16 mm along the horizontal x-axis. The resulting spatial chirp is 20.4 mm/nm, and the spatial distribution of wavelengths is modeled as $x_1(\lambda) = 20.4(\lambda - 796)$ mm.

B. Spectral transformation

1. *Methodology*

This *spectral* transformation can be achieved via a two-to-one *spatial* coordinate transformation performed along the horizontal x-axis. Because the wavelengths are arranged linearly along x after the *spectral analysis* stage and the field is uniform along y, this 1D coordinate transformation re-arranges the wavelengths along x, thereby producing the targeted spectral transformation. This spectral transformation stage aims at achieving two goals: (1) dynamically reconfiguring the wavelength arrangement in the spatially resolved spectrum (which will subsequently result in tuning the surface of the spatiotemporal spectrum of the ST meron); and (2) performing a two-to-one mapping of wavelengths, thereby assigning *two* wavelengths to each position along the x-axis at the output plane, in contrast to the field at the input plane in which each position is associated with a *single* wavelength. This latter feature opens the path towards realizing ST merons on a closed-surface spatiotemporal spectrum. In general, combining this *spectral transformation* stage with the *spectral analysis* stage, we can produce, in principle, an arbitrary sequence of wavelengths, which will subsequently produce an arbitrary spatiotemporal spectral surface.

The x-axis at the input plane is labeled x_1 and x_2 at the output plane. The targeted transformation then takes the form:

$$x_2 = A \ln\left|\frac{x_1(\lambda)}{B}\right|, \tag{9a}$$

$$y_2 = y_1, \tag{9b}$$

where A and B are scaling parameters at the input and output planes, respectively, and the uniform field distribution along y remains intact. According to Eq. 9, a pair of points at $\pm x_1$ in the input plane are mapped to the same point x_2 in the output plane, thus yielding a two-to-one spatial transformation. To the best of our knowledge, all previous attempts at conformal transformations have been limited to only one-to-one mappings [12–15], and thus fall short of attaining the transformation in Eq. 9. In our approach, we divide the transformation in Eq. 9 into two one-to-one mappings:

$$T^{(+)}: x_2 = A\ln(x_1/B);\ x_1 > 0, B > 0, \tag{10a}$$

$$T^{(-)}: x_2 = A\ln(x_1/B);\ x_1 < 0, B < 0. \tag{10b}$$

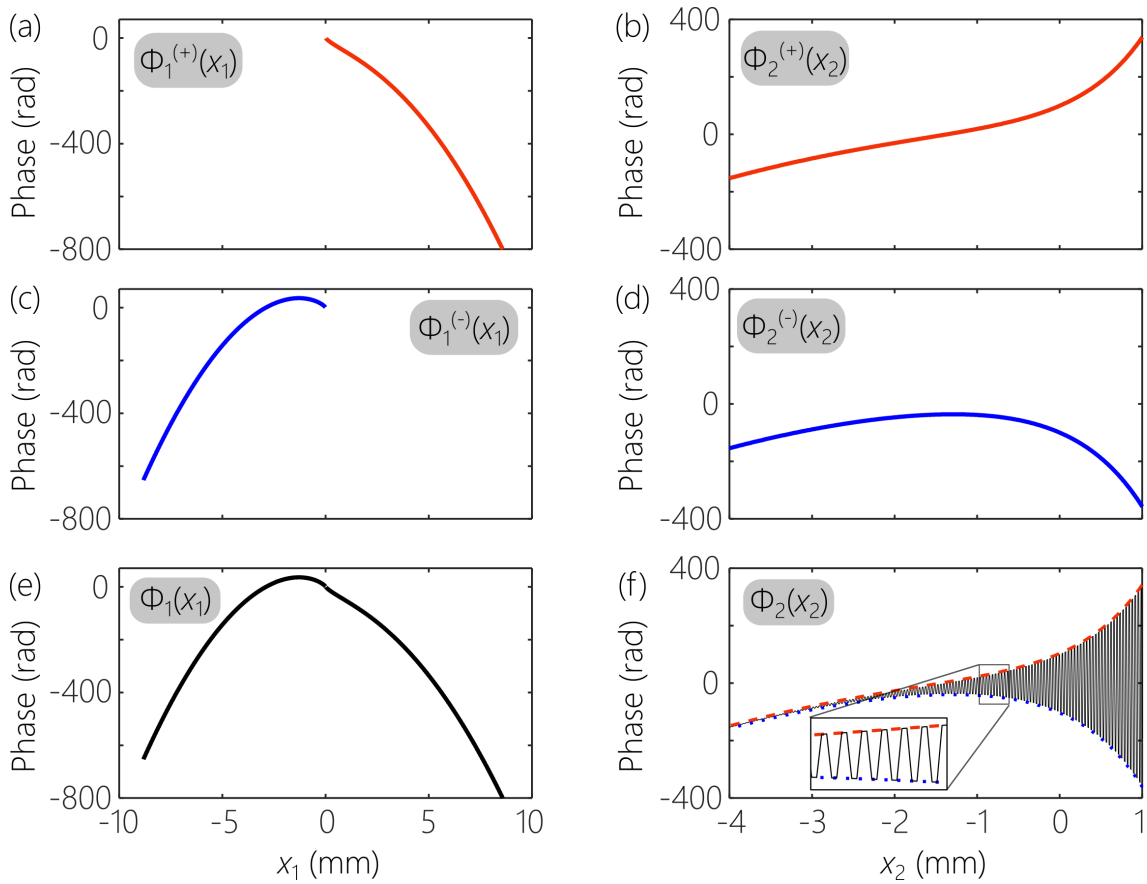

FIG. S4. The phase profiles required to implement the spectral transformation. (a) The phase profiles $\Phi_1^{(+)}(x_1)$ and (b) $\Phi_2^{(+)}(x_2)$ to perform one-to-one transformation $T^{(+)}$ corresponding to $x_2{=}A\ln(x_1/B)$ for $x_1{>}0$ and $B{>}0$. (c) The phase profiles $\Phi_1^{(-)}(x_1)$ and (d) $\Phi_2^{(-)}(x_2)$ to perform the one-to-one transformation $T^{(-)}$ corresponding to $x_2{=}A\ln(x_1/B)$ for $x_1{<}0$ and $B{<}0$. (e) The phase profile $\Phi_1(x_1)$ in the input plane to implement the two-to-one transformation T corresponding to $x_2{=}Ax_1\ln|x_1/b|$, which results from *concatenating* the phase profiles in (a) and (c). (f) The phase profile $\Phi_2(x_2)$ in the output plane obtained by *interleaving* the phase patterns in (b) and (d) every two pixels. The inset enlarges the plot in the range $-1\text{mm}{<}x_2{<}-0.5\text{mm}$.

The two transformations $T^{(+)}$ and $T^{(-)}$ are assigned to different non-overlapping domains of the input plane $x_1{>}0$ and $x_1{<}0$, respectively, but share the same output domain x_2. We can thus use the existing methodologies to obtain the phase profiles required to perform each of these two transformations. Such one-to-one conformal mapping can be implemented using two phase patterns placed at the input and output planes and separated by a distance d_1. The first phase distribution $\Phi_1(x_1)$ at the input plane performs the desired transformation. However, such a

transformation does not produce a collimated field. The second phase distribution $\Phi_2(x_2)$ placed at the output plane collimates the transformed wavefront to yield an afocal transformation. The required phase profiles can be derived using the methodology outlined in [13]. For the $T^{(+)}$ mapping the required phase profiles $\Phi_1^{(+)}(x_1)$ and $\Phi_2^{(+)}(x_2)$ take the form:

$$\Phi_1^{(+)}(x_1) = \frac{kA}{d_1}\left[x_1 \ln\left(\frac{x_1}{B}\right) - x_1\right] - \frac{kx_1^2}{2d_1}, \tag{11a}$$

$$\Phi_2^{(+)}(x_2) = \frac{kAB}{d_1}\exp\left(\frac{x_2}{A}\right) - \frac{kx_2^2}{2d_1}, \tag{11b}$$

where $k = \frac{2\pi}{\lambda}$ is the wave number, $x_1 > 0$ and $B > 0$ [Fig. S4 (a,b)] For the $T^{(-)}$ mapping the required phase profiles $\Phi_1^{(-)}(x_1)$ and $\Phi_2^{(-)}(x_2)$ are

$$\Phi_1^{(-)}(x_1) = \frac{kA}{d_1}\left[x_1 \ln\left(\frac{x_1}{B}\right) - x_1\right] - \frac{kx_1^2}{2d_1}, \tag{12a}$$

$$\Phi_2^{(-)}(x_2) = -\frac{kAB}{d_1}\exp\left(\frac{x_2}{A}\right) - \frac{kx_2^2}{2d_1}, \tag{12b}$$

where $x_1 < 0$ and $B < 0$ [Fig. S4 (c,d)] . Now we need to combine these transformations into one to perform both of them at the same time. For that, we need to combine $\Phi_1^{(+)}(x_1)$ and $\Phi_1^{(-)}(x_1)$ into one $\Phi_1(x_1)$, which is straightforward as they have non-overlapping input spaces $x_1 > 0$ and $x_1 < 0$ [Fig. S4 (e)]. It is more challenging to combine $\Phi_2^{(+)}(x_2)$ and $\Phi_2^{(-)}(x_2)$ into one $\Phi_2(x_2)$ as they share the same parameter space x_2. We achieve this by interleaving these two phase patterns every two pixels so the field interacts with both profiles at the same time [Fig. S4 (f)]. Note that such a method of combination by interleaving leads to finite diffraction efficiency, where undesired diffraction orders can be cleared out by subsequent spatial filtering that follows the transformation.

2. *Experimental implementation*

In the setup, the two phase distributions $\Phi_1(x_1, y_1)$ and $\Phi_2(x_2, y_2)$ are imparted to the optical field via two reflective, phase-only spatial light modulators (SLMs; Meadowlark 1920×1080 series). The SLMs are operated at a 5° incidence angle and are separated by d_1=400 mm. Because the phase profiles depend only on x and not y, 1D SLMs can – in principle – be used instead. However, utilizing 2D SLMs provides the possibility of also modulating the field along y, which can be

exploited to inculcate a phase modulation that is converted to the azimuthal coordinate after the subsequent *coordinate transformation*. In our experiments, we use A=0.8 mm and $|B|$=6.5 mm for the double-paraboloid ST meron, and A=−1.5 mm and $|B|$=0.5 mm for the spinning-top ST meron.

The field after this spectral transformation is imaged by a $4f$ system with unity magnification comprising two spherical lenses from the output plane of the spectral transformation (x_2,y_2) to the input plane (x_3,y_3) of the coordinate transformation. The field is flipped along the x and y axes: $x_3=-x_2$ and $y_3=-y_2$. In addition, a spatial filter (in the form of a beam stop) is placed in the Fourier plane of the $4f$ system to eliminate the undesired zeroth-order field component resulting from the limited efficiency of SLM_1 and SLM_2.

C. Coordinate transformation

1. *Methodology*

In this coordinate-transformation stage, conformal mapping is performed from log-polar to Cartesian coordinate systems. The input plane is spanned by Cartesian coordinates (x_3,y_3) and the output by (x_4,y_4). The transformation maps the input Cartesian coordinate system (x_3,y_3) to a polar coordinate system at the output: $(x_3,y_3)\rightarrow(r,\varphi)$, where $r=\sqrt{x_4^2+y_4^2}$ and $\varphi=\arctan(\frac{y_4}{x_4})$. The transformation is given explicitly as follows [12, 13, 16]:

$$r=C\exp\left(-\frac{x_3}{D}\right), \tag{13a}$$

$$\varphi=\frac{y_3}{D}. \tag{13b}$$

The transformation parameter D is chosen to map the vertical coordinate y_3 of the input field, which extends over the range $y_3=[-y_3^{\max},y_3^{\max}]$ to the angular range $\varphi=[-\pi,\pi]$, which requires that $D=\frac{y_3^{\max}}{\pi}$. The value of C is selected based on the radial aperture size of the optics used. This coordinate transformation therefore maps a vertical line located at x_3 at the input plane into a circle of radius $r=C\exp\left(-\frac{\pi x_3}{y_3^{\max}}\right)$ at the output plane.

This coordinate transformation is implemented by two 2D phase plates separated by a distance d_2. The first plate introduces the phase distribution $\Phi_3(x_3,y_3)$ at the input plane, and the second

introduces the phase distribution $\Phi_4(x_4,y_4)$ at the output plane. For the mapping given in Eq. 13, the phase patterns take the following form [13–15]:

$$\Phi_3(x_3,y_3) = -\frac{kCD}{d_2}\exp\left(-\frac{x_3}{D}\right)\cos\left(\frac{y_3}{D}\right) - \frac{k(x_3^2+y_3^2)}{2d_2}, \tag{14a}$$

$$\Phi_4(x_4,y_4) = \frac{kD}{d_2}\left[\text{atan2}(y_4,x_4) - x_4\ln\left(\frac{\sqrt{(x_4^2+y_4^2)}}{C}\right) + x_4\right] - \frac{k(x_4^2+y_4^2)}{2d_2}, \tag{14b}$$

where atan2(y_4,x_4) is the 2-argument arctan function. This arctan function generates a phase singularity at $x_4=y_4=0$ in Eq. 14b, which would lead to a null intensity around $r=0$. This is not surprising as according to Eq. 13a we expect to asymptotically reach $r\to 0$ at $x_3\to\infty$. In a widespread application of the log-polar coordinate transformation – sorting orbital-angular-modes (OAM) when operated in a reverse geometry – this singularity usually escapes attention because the incident field typically has a central node resulting from the helical nature of OAM wavefronts. In other words, for OAM sorting, a circularly symmetric field with a null intensity at the center is incident on the second phase plate, which veils the phase singularity in the second phase plate [Eq. 14b].

2. *Design of the phase profiles*

We designed a phase plate to perform the coordinate transformation with the minimal effect of the intensity null around $r=0$ discussed above. We optimize the transformation parameter C, separation d_2 in Eq. 13 and the aperture of the phase plates to maximize the ratio of the outer radius r_{out} to the inner radius r_{in}, i.e. $R=r_{\text{out}}/r_{\text{in}}$. On the other hand, while maximizing R, we need to make sure that during the transformation we stay within the paraxial regime as the phase profiles in Eq 14 work well only within the paraxial regime. After taking into account all these points, we find that the optimal ratio of $R=40$ is achieved for the aperture size of 14×14 mm^2, the separation distance of $d_2=300$ mm, transformation parameters of $C=7$ mm and $D=\frac{12.37}{2\pi}\approx 2$ mm for the central wavelengths of $\lambda=798$ nm.

3. *Fabrication of diffractive phase plates for the coordinate transformation*

We use a pair of analog diffractive optics [17] that introduce the phase profiles given in Eq. 14 modulo 2π to implement the coordinate transformation. Fabrication of the diffractive elements

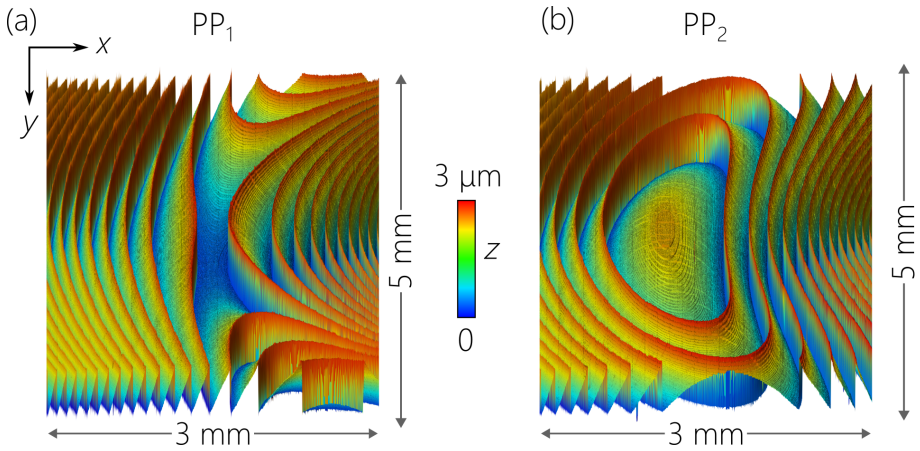

FIG. S5. Surface profiles of the diffraction phase plates to implement the coordinate transformation. Analog log-polar mode sorting optics that consist of (a) a transformation optic and (b) a phase-correcting optic.

was performed using an analog photolithographic process [18, 19]. The complex phase function is converted to a surface profile in photoresist using a mapping that corresponds to the desired optical phase-only element. This intensity profile is then mapped to the zero-order diffraction of a slowly varying phase mask with binary phase values 0 and π. This mask is then placed into a 5× reduction projection printer (GCA – ALS, 0.45 NA, λ=365 nm), where all the non-zero diffraction orders are filtered in the pupil plane, leaving only the zero-order intensity variation in the wafer plane that is used to expose the photoresist. The photoresist (SPR220-3.0) has an initial thickness of 3.5 um, which is reduced to 2.6 um after exposure, was subsequently developed using AZ 300 MIF developer, and then post-exposure baked. This pattern was then transfer etched into a fused silica substrate using CHF_3 and O_2 gas chemistry for a resulting overall etch thickness corresponding to a 2π phase depth for λ=798 nm, which was ≈1760 nm.

The 5× de-magnification requires recording a mask of size 70×70 mm^2 to produce an analog phase plate of 14×14 mm^2 surface area. The unusually large size of the masks necessitated a recording time for the phase mask to produce Φ_3 in Eq. 14(a) [Fig. S5(a)] was ≈2 days and the recording time for the phase mask for Φ_4 in Eq. 14(b) [Fig. S5(b)] was ≈4 days. We depict in Fig. S5 the profiles of the two fabricated diffractive elements captured using a Keyence VK-X3000 confocal microscope with a 50× microscope objective. The 4800×2700 µm^2 area shown for each optic was captured by stitching together adjacent images.

D. Metasurface for implementing a meron spin-texture

We introduce the meron texture in the spectral (k_x,k_y,λ)-domain by placing the meron metasurface immediately after the *coordinate transformation*, before the final Fourier-transforming lens in the synthesis setup (Fig. S2). The metasurface is specially designed to introduce a meron texture into a field when the incident light is polarized at 45°, so we place the optical axis of the metasurface at 45° with respect to the horizontal axis, which corresponds to the polarization state emerging from the earlier stages. We designed a metasurface of surface area 14×14 mm^2 to correspond to the spatial extent of the field emerging from the *coordination transformation* stage which is ≈14 mm.

1. *Metasurface design*

The target polarization profile depicted in Fig. S6(a), which constitutes the spin-texture of a meron quasi-particle, corresponds to x- and y-polarized components of the form:

$$E_x = \tan\frac{\theta}{2}+e^{i\varphi}, \tag{15}$$

$$E_y = i\left(\tan\frac{\theta}{2}-e^{i\varphi}\right), \tag{16}$$

where φ is the azimuthal coordinate and θ is given by:

$$\theta=\pi-\frac{\kappa}{\sqrt{x^2+y^2+\kappa^2}}, \tag{17}$$

and we set $\kappa=1$ mm here. The amplitude and phase profiles of the E_x and E_y field components are plotted in Fig. S6(b,d) and Fig. S6(c,e), respectively.

As described in the main text, we modulate the spatial distribution of the field polarization to produce the desired polarization texture using a dielectric birefringent metasurface. We adopt a holographic-based phase-retrieval-like algorithm [20–23] to realize the target complex amplitude profiles defined in Eq. 15 and Eq. 16. The phase-only profiles required to fully reconstruct E_x and E_y (following Eq. (16) of Ref. [24]) are depicted in Fig. S6(f,g). We refer to these phases as CGH$_x$ and CGH$_y$ since they are essentially two independent computer-generated holograms (CGHs).

The next step is to fit the phase profiles CGH$_x$ and CGH$_y$, pixel-by-pixel, into the birefringent meta-atoms (unit cells) of a metasurface. Figure S7 depicts the meta-atom geometry that we adopted for this task. It is composed of an 800-nm-tall rectangular titanium dioxide (TiO_2) nanofin

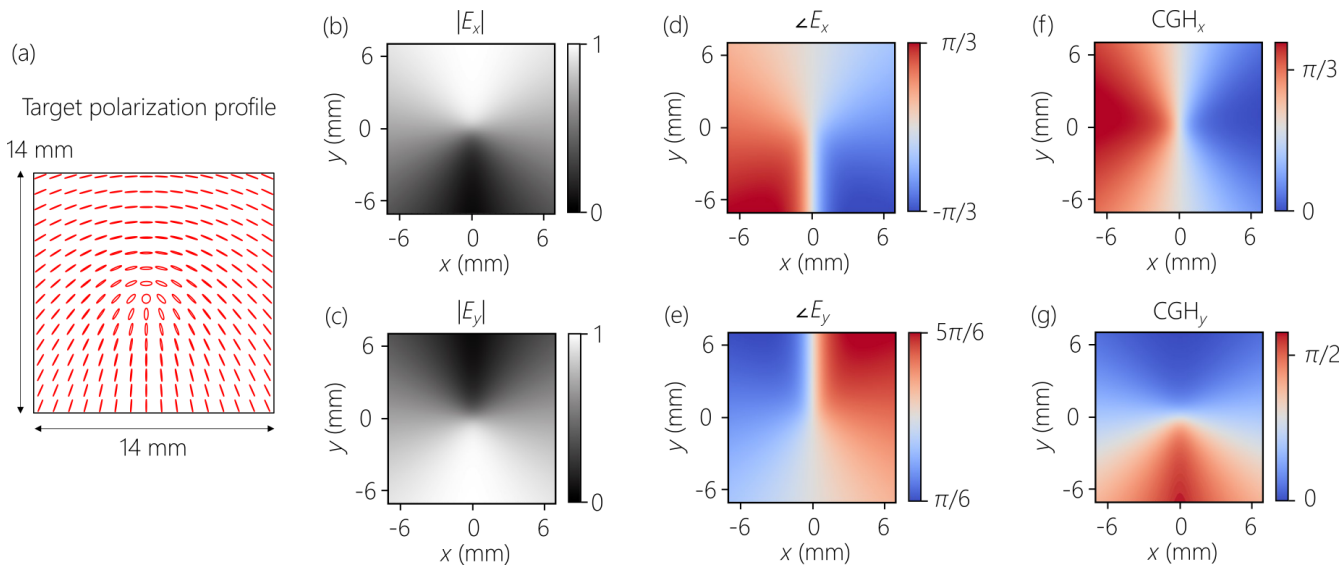

FIG. S6. Phase retrieval of the metasurface plane. (a) The target polarization profile is described by the spatially varying polarization ellipses depicted in red. This polarization profile is decomposed into two orthogonal field components, E_x and E_y. The amplitude of (b) the x-polarized field $|E_x|$ and (c) the y-polarized field $|E_y|$. The phase of (d) the x-polarized field ϕ_x and (e) the y-polarized field ϕ_y. The phase-only profiles for (f) the x-polarized and (g) y-polarized light needed for the holographic reconstruction of the target polarization profile shown in (a).

on a silica substrate. This choice of tall nanofins is amenable to our fabrication process while enabling full-phase coverage at the design wavelength, as shown below. The unit cell size is 520×520 nm^2. By changing the length d_x and width d_y of each nanofin, light polarized along the x and y directions experience different effective refractive indices, thereby accruing different phase delays.

The phase and amplitude of the transmission response of an x-polarized plane wave propagating through the nanofin as a function of d_x and d_y are shown in Fig. S8(a,b), respectively. The phase shift and transmission responses were obtained numerically via FDTD simulations. The phase shift was obtained by probing the center of the far field projection on a plane above the structure, whereas the power transmission here is defined as the total power passing through a monitor above the structure relative to the source. We refer to this map as the metasurface 'look-up table' or 'library.' To better visualize the phase coverage of our metasurface library, we plot the complex transmission $t_x e^{i\varphi_x}$ as depicted in Fig. S8(c). Each blue dot refers to a unique

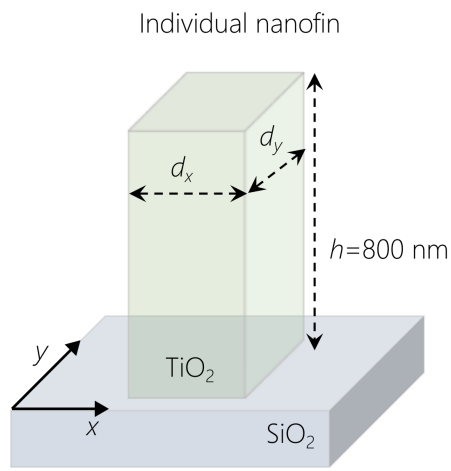

FIG. S7. Metasurface unit cell. Schematic of the metasurface unit cell composed of a rectangular nanofin made of titanium dioxide (TiO_2) with a fixed height of 800 nm on top of a glass substrate. These unit cells support two propagating modes which, due to anisotropy, experience different indices (phase delays).

nanofin geometry. The plot suggests that our metasurface library has sufficient meta-atoms to trace a unit circle, which implies full $0-2\pi$ phase coverage.

After populating the library, the next task is to fit the phase profiles CGH_x and CGH_y into the physical meta-atoms; hence, constructing the metasurface mask. The selection criteria for this mapping are performed pixel-by-pixel across the profile of the metasurface. It is a three-step process which is described as follows [25]: (a) The complex-valued errors ϵ_x and ϵ_y are first evaluated from

$$\epsilon_x = |t_{\mathrm{avg}} e^{i\varphi_{x,\mathrm{des}}} - t_{\mathrm{sim}} e^{i\varphi_{x,\mathrm{sim}}}|, \tag{18}$$

$$\epsilon_y = |t_{\mathrm{avg}} e^{i\varphi_{y,\mathrm{des}}} - t_{\mathrm{sim}} e^{i\varphi_{y,\mathrm{sim}}}| \tag{19}$$

for all possible nanofin configurations. (b) For each geometry spanning across the metasurface geometry, the maximum error $\epsilon_{\mathrm{max}} = \max(\epsilon_x, \epsilon_y)$ is determined, and finally (c) the configuration that minimizes ϵ_{max} at that pixel is selected. This process is iteratively repeated point-by-point at each location of the metasurface until the entire mask is obtained. In essence, 45° linearly polarized light incident on the nanofin can be decomposed into x- and y-polarized components of equal magnitudes. After a single interaction with the metasurface, these two orthogonal polarization components will be encoded with the desired phase profiles CGH_x and CGH_y, achieving the target polarization transformation.

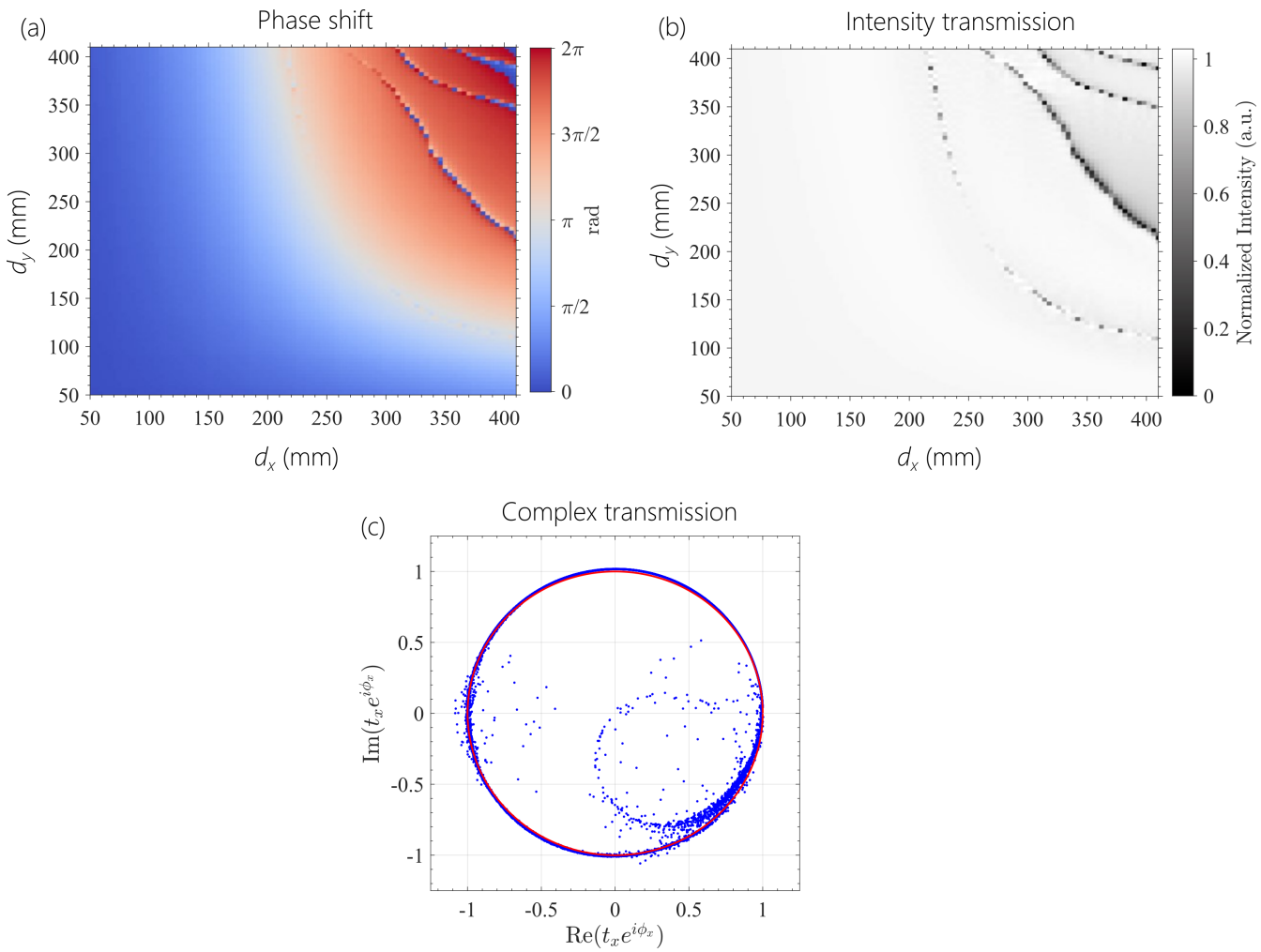

FIG. S8. Metasurface Library. (a) Phase response ϕ_x of the nanofin (in Radians) as a function of the transverse dimensions, d_x and d_y, for incident x-polarization. (b) The normalized power transmission of the nanofins as a function of d_x and d_y, for x-polarization. From the symmetry of the rectangular structure, y-polarization response is readily obtained by swapping x and y in (a) and (b). (c) The electric field amplitude transmission $t_x e^{i\phi_x}$ plotted on the complex plane for each of the 2600 individual geometries (blue dots). The red circle is the unit circle implying that our library can provide unity transmission and phase coverage.

2. *Metasurface fabrication*

Once the metasurface profile is obtained, a CAD file is then generated and the metasurface is fabricated using standard cleanroom recipes. Given the large size of the metasurface (14×14 mm^2 surface area) and its subwavelength pixel pitch (520 nm), the CAD design contains roughly 725

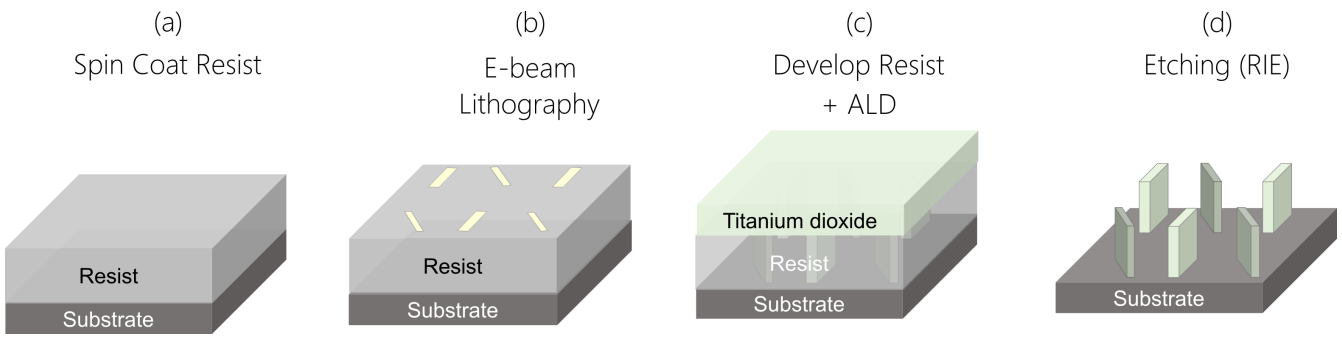

FIG. S9. Metasurface fabrication using a bottom-up approach. (a) A silica substrate is spin-coated with an e-beam resist. (b) The resist is baked and then nanopatterned using e-beam lithography. (c) After developing the resist, the nanopatterned gaps are conformally filled with TiO_2 using atomic layer deposition (ALD). (d) Finally, the excess film is etched away using reactive ion etching (RIE), and the resist is removed, leading to the final structure.

million nanofins. Handling this amount of data in a single CAD file is not feasible by state-of-the-art benchtop computers due to memory constraints. Therefore, the target design was fragmented into 56 strips of 0.25 mm by 1.4 cm, each stored in a separate CAD file before their final assembly on the lithography tool. While a 2-cm Pancharatnam-Berry phase metalens (made of rectangular nanofins of the same dimensions) has been previously reported for light focusing [26], our 14-mm device represents the largest metasurface for shaping vectorial structured light to date. The final device was fabricated using a process reliant on electron beam lithography and atomic layer deposition, as shown in Fig. S9 and described more fully in Ref. [27, 28]. The procedure is as follows: a fused silica substrate is first spin-coated with a positive tone electron beam resist (ZEP520A, Zeon SMI) that ultimately defines the height of the nanofins (800 nm). After baking the resist, the desired pillar patterns were written by exposing the resist using electron beam lithography (with an accelerating voltage of 150 kV), then developed in O-Xylene for 60 s. The developed pattern defines the geometry of the individual nanopillars. Afterward, TiO_2 was deposited via the atomic layer deposition process (ALD) to conformally fill the developed pattern. The excess layer of TiO_2 on top of the device was etched away using reactive ion etching to the original height of the resist. Finally, the resist was removed using a downstream ashing (oxygen radicals) process leaving the individual TiO_2 nanopillars surrounded by air. Figure S10 displays sample scanning electron microscope (SEM) images of the fabricated device, confirming its smooth surface and vertical sidewall profile.

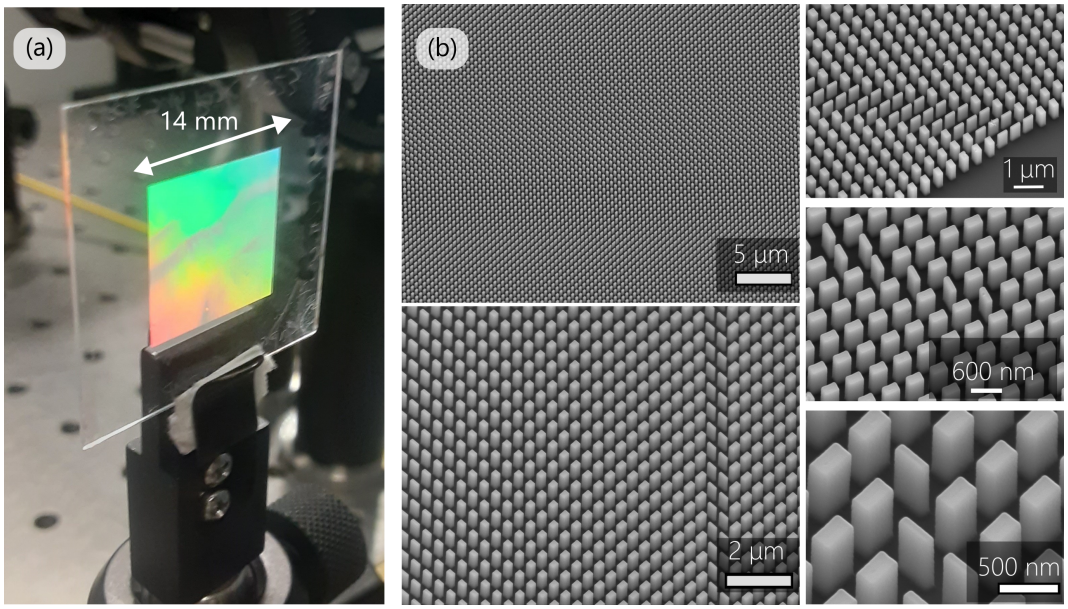

FIG. S10. (a) A photograph and (b) scanning electron microscope (SEM) micrographs of the fabricated metasurface.

3. *Metasurface characterization*

To characterize the device, we used a standard holographic setup comprising a $4f$ imaging system, as shown in Fig. S11. First, a $\lambda = 800$ nm laser beam was spatially filtered and collimated to provide a quasi-plane-wave illumination on the metasurface. A polarizer and HWP rotate the incident polarization so that the metasurface behavior can be measured in response to 45° linearly polarized light. A $4f$ system, comprising two lenses, was used to filter and image the response of the metasurface onto a CCD camera. Lens 1 performs the Fourier operation required to retrieve the complex (amplitude and phase) spectrum of the signal in k-space. The generated Fourier spectrum (at the focal plane of lens 1) was filtered in k-space from higher diffraction orders (using an iris) before it was transformed back to real space via an inverse Fourier operation performed by lens 2. The output beam with its desired polarization behavior was then recorded using a CCD camera positioned at the output focal plane of lens 2 ($z = 0$ plane). To characterize the polarization behavior of the output beam, we performed polarization measurements based on Stokes polarimetry. This enabled the determination of the full, four-component polarization Stokes vector, which quantifies the shape and orientation of the polarization ellipse at each point as well as the beam's intensity and degree of polarization. The Stokes parameters were obtained

by rotating a polarizer and a QWP before the CCD to analyze for different polarization states: 0°,45°,90°,135°, LCP and RCP.

The measured spatial distributions of Stokes parameters in Fig. S11(b) are in close resemblance with the theoretical expectations (Fig. S11(c)). We anticipate that the deviation of the imparted polarization transformation from the target response stems in part from imperfections in the metasurface fabrication as well as the design limitations. Specifically, the retardance of nanofins comprising the meta-atom library was simulated under the assumption of periodic boundary conditions, which is not entirely valid as the target polarization response is spatially varying. The deviation from this assumption, particularly significant near the edge of the metasurface, along with small variations in the actual nanofin dimensions, can collectively lead to undesired residual shape-induced birefringence that distorts the intended retardance of the individual nanofins.

III. CHARACTERIZATION OF ST MERONS

A. Spatio-temporal spectral intensity

The plane at which the metasurface is placed in the setup corresponds to the Fourier plane (k_x,k_y) of the synthesized ST merons. To capture the spatiotemporal spectral intensity $I(k_x,k_y;\lambda)=|\widetilde{\psi}(k_x,k_y;\lambda)|^2$, we image the metasurface plane with a $4f$ system (f=300 and f=100 mm lenses) to CCD_2 (The ImagingSource, DMK 33UX178). Meanwhile, we filter out all diffraction orders except for $+1$ generated by the metasurface, as described in Section II D 3. We plot the measured spectral intensity profile $I(k_x,k_y)$ on the surface of the spatiotemporal spectral surface as a colormap (Fig. 3B-D and Fig. 4B-D of the Main text).

Because the camera is not wavelength-sensitive, we reconstruct the temporal spectrum in two steps. We first scan a fiber tip connected to an optical spectrum analyzer (OSA) along the horizontal axis x_1 after the *spectral analysis* stage and determine the spatial chirp $x_1(\lambda)$, as described earlier in Section II A 2 and Fig. S3(b). In the second step, we verify experimentally the combined impact of the *spectral transformation* and the *coordinate transformation* by scanning a vertical slit horizontally along x_1 and measuring the radius $r(x_1)$ of the annulus formed at the output of the coordinate transformation. By combining these two measurements, we obtain the spatial chirp along the radial direction $r(\lambda)$ after the combined spectral and coordinate transformations. Finally, we obtain spatiotemporal spectrum $k_r(\lambda)$ by converting from the

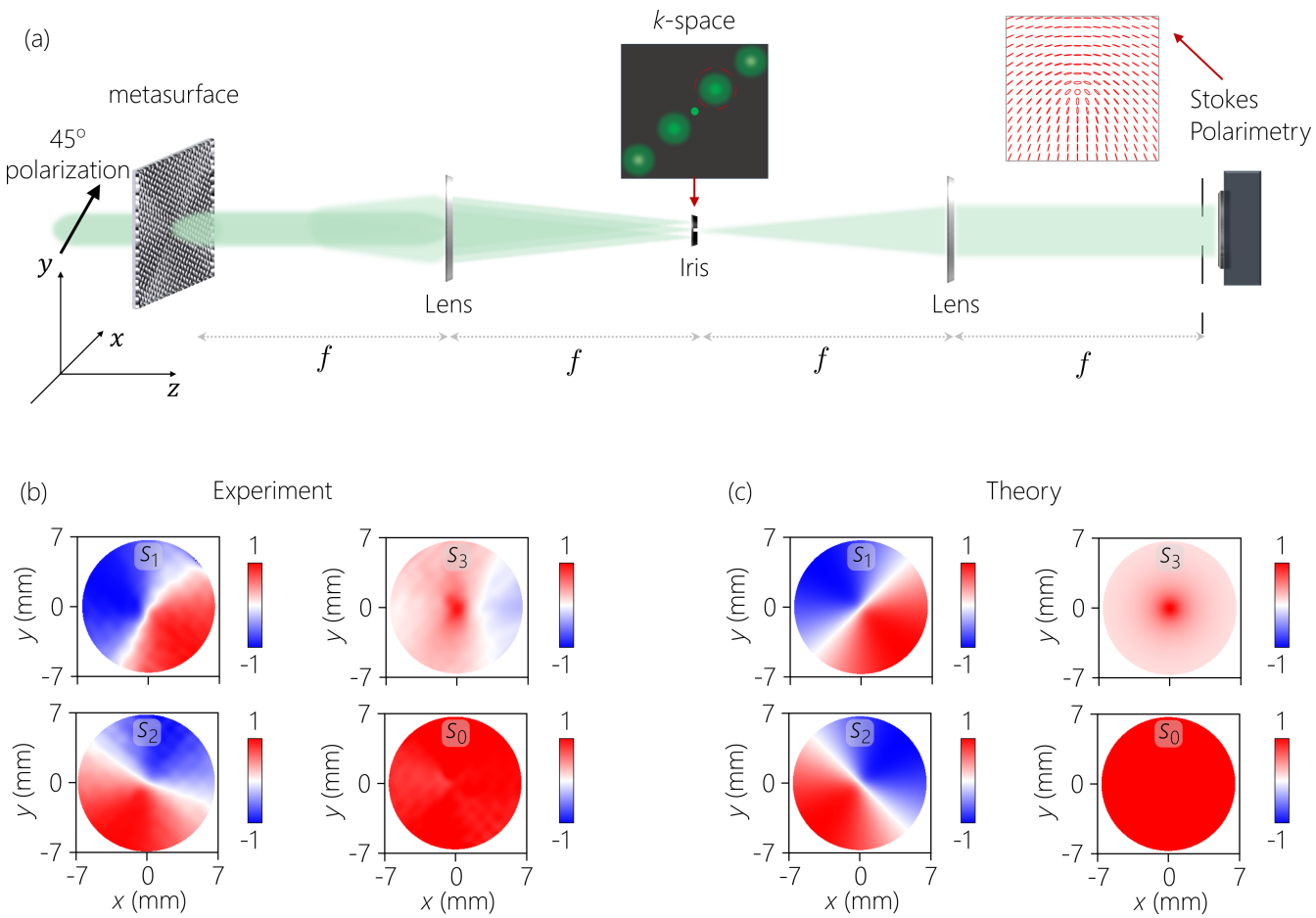

FIG. S11. (a) Metasurface optical characterization. The metasurface is illuminated with a linearly polarized quasi-plane wave. Its output response is filtered and imaged using a 4-f lens system onto a Stokes polarimeter which comprises a polarizer and QWP in front of a CCD sensor to measure the full Stokes parameters (and polarization response) of the device. (b) Experimentally measured Stokes parameters of the metasurface and (c) corresponding theoretical calculations.

physical space to Fourier space $k_r = k\frac{r}{f}$, where $k = \frac{2\pi}{\lambda}$ is the wave number, and f=300 mm is the focal lens of the Fourier-transforming lens. Using measurements of $\lambda(k_r)$ obtained this way, we plot 3D spatiotemporal spectral surfaces of the ST merons in Fig. 3D and Fig. 4D of the Main text.

This method of course provides the spatiotemporal spectral intensity profile averaged over all polarization states because the camera is polarization-insensitive. We perform Stokes polarimetry in the spectral domain to capture the polarization texture.

B. Spectral Stokes polarimetry

To characterize the polarization texture of ST merons in the spectral domain, we carry out spatially-resolved Stokes polarimetry in the Fourier plane (k_x,k_y) as mentioned above. We use a conventional setup for Stokes polarimetry [4] comprising a polarising beam splitter (PBS, Thorlabs PBS252) projecting the polarization into two orthogonal states, a pair of cameras CCD_1 and CCD_2 (The ImagingSource, DMK 33UX178) capturing both ports of the PBS, a half-wave plate (HWP), and a quarter-wave plate (QWP) to modify the basis for polarization analysis. Using this configuration, we measure the spectral intensity of the field $I(k_x,k_y,\lambda)$ corresponding to the polarization states H (horizontally polarized), V (vertically polarized), $+45°$,$-45°$, RCP (right circularly polarized), and LCP (left circularly polarized), from which we calculate normalized Stokes parameters $s_0(k_x,k_y,\lambda)$,$s_1(k_x,k_y,\lambda)$,$s_2(k_x,k_y,\lambda)$ and $s_3(k_x,k_y,\lambda)$ in the spectral domain (Fig. 3A and Fig. 4A, first row). The measured Stokes parameters match the target profiles shown in the second row of Fig. 3A and Fig. 4A.

Subsequently, in Fig. 3b-d and Fig. 4b-d (arrows), we represent the polarization texture of the ST merons via a three-component unit vector field $\boldsymbol{n}(k_x,k_y,\lambda)$ as defined in Eq. 2 [29, 30]. From the plots of polarization texture in Fig. 3b and Fig. 4b the qualitative resemblance of the meron texture is clear – $\hat{n}=\hat{z}$ near the center $k_r=0$, and $\hat{n}\perp\hat{z}$ near the edges $k_r=k_r^{\max}$, as discussed in Section I and Fig. S1. For a quantitative comparison of the measured polarization texture with the target meron texture we calculate the Skyrmion number using a topological method described in the next section [31]. Using this method, we measure the Skyrmion number of $Q=0.43$ for the double-paraboloid ST meron (Fig. 3b, inset) and $Q=0.41$ for the spinning-top ST meron (Fig. 4b, inset), both of which are very close to the target value of $Q=0.5$ for a meron quasi-particle.

C. Extracting Skyrmion number from the measurements of Stokes parameters

We extract the Skyrmion number from the measurements of Stokes parameters s_1,s_2,s_3 using a topological method introduced for paraxial optical skyrmions [31]. The Skyrmion number is calculated via a line integral around the intensity singularity point as opposed to the gradient of the polarization texture, which improves the accuracy of measurement as the gradient is limited

within the aperture of the experimental system and is extremely sensitive to noise. Following this method, we determine the Skyrmion number

$$Q=\frac{1}{2}\left(\sum s_3^{(j)}N^{(j)}-s_3^{(\infty)}N^{(\infty)}\right), \tag{20}$$

where $N=(2\pi)^{-1}\oint\nabla\Phi\cdot d\mathbf{l}$ is the winding number at the jth inner singularity and at the beam periphery (∞), $s_3^{(j)}$ and $s_3^{(\infty)}$ are the Stokes parameter s_3 at these two locations, and $\Phi=\arg(s_1+is_2)$ [31]. Singularities are located where $s_1,s_2\rightarrow 0$ and within the context of our work there is only one singularity $j=1$ located at the beam center, as seen in Fig. S11 (b). We evaluate $s_3^{(1)}$ by averaging over a square of 10×10 pixels centered at the location of the singularity, whereas $s_3^{(\infty)}$ is calculated by averaging the values of s_3 lying along a circular path near the edge of the beam centered on the beam center. The winding number N in Eq. 20 describes the number of turns completed by $\boldsymbol{n}$ on the Poincaré sphere along a path surrounding the singularity. Computationally, plotting the Stokes phase Φ reveals the location of singularities and the corresponding winding numbers. We determine N by counting the number of peaks in the angular direction of the polar plot of Φ around the singularity ($N^{(1)}$) and near the edge of the beam ($N^{(\infty)}$).

Using this methodology, we extract the Skyrmion number from the experimental data of the birefringent metasurface (Fig. S11(b)), open-surface ST meron (Fig. 3(a) of the Main text), and a close-surface ST meron (Fig. 4(a) of the Main text). In Fig. S11(b) we choose the periphery circle of radius $r^{(\infty)}\approx 6.1$ mm and obtain Skyrmion number of $Q\approx 0.416$, which is very close to the theoretically expected number of $Q_{\text{th}}=0.418$ from Eq. 15-17. We anticipate that the source of a slight deviation of $\delta Q\approx 0.02$ is an imperfection in metasurface fabrication described above. For the open-surface (Fig. 3(a)) and closed-surface ST meron (Fig. 4(a)), we select $k_r^{(\infty)}\approx 150$ rad/mm and obtain a Skyrmion number of $Q\approx 0.41$ and $Q\approx 0.42$ respectively. Note that for the polarization distribution in the form of Eq. 15,16 the Skyrmion number of $Q=0.5$ would be obtained for $k_r^{(\infty)}\rightarrow\infty$. Alternatively, one could design a different polarization distribution function that would result in $Q=0.5$ at the edge of a finite beam.

D. Spatiotemporally resolved Stokes polarimetry

We measure the spatio-temporal evolution of the polarization texture of ST merons in the physical space by carrying out Stokes polarimetry in the common path of the Mach-Zehnder interferometer (Fig. S2). In the first (reference) arm of the interferometer, we have the initial 100-fs

linearly polarized plane-wave pulse from the input laser passing through a controllable optical delay line τ and half-wave plate (HWP). In the second arm, we place the ST meron synthesis setup that produces an optical field with a nontrivial polarization profile. When two wave packets are combined using a beam splitter to co-propagate collinearly, we observe spatially-resolved interference fringes on the CCD_3 (TheImagingSource, DMK 27BOP031), and from the visibility of fringes, we calculate the intensity profile of the ST meron [11, 32]. To maximize the interference fringes, we place a linear polarizer in front of CCD_3, which projects both pulses into one polarization state [33]. By sweeping the delay line τ, we record a collection of spatially-resolved intensity profiles and construct spatio-temporally resolved intensity profile $I_P(x,y;\tau)$ of the ST meron projected into the certain polarization state. We repeat the procedure for different polarization states (H, V, $+45°$,$-45°$, RCP, and LCP) via rotating the axis of the polarizer and using HWP/QWP to measure all four spatio-temporally resolved Stokes parameters, i.e. $s_i(x,y;\tau)$ for i=0,1,2 and 3. For better visualization, in Fig. 3E and Fig. 4E, we show 2D plots of Stokes parameters at y=0 cross-section.

---

[1] S. Tsesses, E. Ostrovsky, K. Cohen, B. Gjonaj, N. H Lindner, and G. Bartal, "Optical skyrmion lattice in evanescent electromagnetic fields," Science **361**, 993–996 (2018).

[2] L. Du, A. Yang, A. V. Zayats, and X. Yuan, "Deep-subwavelength features of photonic skyrmions in a confined electromagnetic field with orbital angular momentum," Nat. Phys. **15**, 650–654 (2019).

[3] Y. Dai, Z. Zhou, A. Ghosh, R. S. K. Mong, A. Kubo, C. Huang, and H. Petek, "Plasmonic topological quasiparticle on the nanometre and femtosecond scales," Nature **588**, 616–619 (2020).

[4] B. E. A. Saleh and M. C. Teich, *Principles of Photonics* (Wiley, 2007).

[5] S. Kaim, S. Mokhov, B. Y. Zeldovich, and L. B. Glebov, "Stretching and compressing of short laser pulses by chirped volume Bragg gratings: analytic and numerical modeling," Opt. Eng. **53**, 051509 (2014).

[6] L. B. Glebov, V. Smirnov, R. Eugeniu, I. Cohanoschi, L. Glebova, O. V. Smolski, J. Lumeau, C. Lantigua, and A. Glebov, "Volume-chirped Bragg gratings: monolithic components for stretching and compression of ultrashort laser pulses," Opt. Eng. **53**, 051514 (2014).

[7] K. Liao, M. Cheng, E. Flecher, V. I. Smirnov, L. B. Glebov, and A. Galvanauskas, "Large-aperture chirped volume Bragg grating based fiber CPA system," Opt. Express **15**, 4876–4882 (2007).

[8] M. Martyanov, I. Mukhin, I. Kuzmin, and S. Mironov, "Compact pulse shaper based on a tilted volume Bragg grating," Opt. Lett. **47**, 557–560 (2022).

[9] O. Mhibik, M. Yessenov, L. Mach, L. Glebov, A. F Abouraddy, and I. Divliansky, "Rotated chirped volume Bragg gratings for compact spectral analysis," Opt. Lett. **48**, 1180–1183 (2023).

[10] M. Yessenov, O. Mhibik, L. Mach, T. M Hayward, R. Menon, L. Glebov, I. Divliansky, and A. F Abouraddy, "Ultra-compact synthesis of space-time wave packets," Opt. Lett. **48**, 2500–2503 (2023).

[11] M. Yessenov, J. Free, Z. Chen, E. G. Johnson, M. P. J. Lavery, M. A. Alonso, and A. F. Abouraddy, "Space-time wave packets localized in all dimensions," Nat. Commun. **13**, 4573 (2022).

[12] O. Bryngdahl, "Geometrical transformations in optics," J. Opt. Soc. Am. **64**, 1092–1099 (1974).

[13] W. J. Hossack, A. M. Darling, and A. Dahdouh, "Coordinate transformations with multiple computer-generated optical elements," J. Mod. Opt. **34**, 1235–1250 (1987).

[14] G. C. G Berkhout, M. P. J. Lavery, J. Courtial, M. W. Beijersbergen, and M. J. Padgett, "Efficient sorting of orbital angular momentum states of light," Phys. Rev. Let. **105**, 153601 (2010).

[15] M. P. J. Lavery, D. J. Robertson, G. C. G Berkhout, G. D. Love, M. J. Padgett, and J. Courtial, "Refractive elements for the measurement of the orbital angular momentum of a single photon," Opt. Express **20**, 2110–2115 (2012).

[16] Y. Saito, S. Komatsu, and H. Ohzu, "Scale and rotation invariant real time optical correlator using computer generated hologram," Opt. Commun. **47**, 8–11 (1983).

[17] W. Li, K. S. Morgan, Y. Li, J. K. Miller, G. White, R. J. Watkins, and E. G. Johnson, "Rapidly tunable orbital angular momentum (OAM) system for higher order Bessel beams integrated in time (HOBBIT)," Opt. Express **27**, 3920–3934 (2019).

[18] J. Sung, H. Hockel, and E. G Johnson, "Analog micro-optics fabrication by use of a two-dimensional binary phase-grating mask," Opt. Lett. **30**, 150–152 (2005).

[19] J. Sung, H. Hockel, J. D Brown, and E. G Johnson, "Development of a two-dimensional phase-grating mask for fabrication of an analog-resist profile," Appl. Opt. **45**, 33–43 (2006).

[20] N. Yu, P. Genevet, M. A. Kats, F. Aieta, J.-P. Tetienne, F. Capasso, and Z. Gaburro, "Light propagation with phase discontinuities: Generalized laws of reflection and refraction," Science **334**, 333–337 (2011).

[21] S. M. Kamali, E. Arbabi, A. Arbabi, and A. Faraon, "A review of dielectric optical metasurfaces for wavefront control," Nanophotonics **7**, 1041–1068 (2018).

[22] N. A. Rubin, Z. Shi, and F. Capasso, "Polarization in diffractive optics and metasurfaces," Adv. Opt. Photon. **13**, 836–970 (2021).

[23] A. H. Dorrah and F. Capasso, "Tunable structured light with flat optics," Science **376**, eabi6860 (2022).

[24] V. Arrizón, U. Ruiz, R. Carrada, and L. A. González, "Pixelated phase computer holograms for the accurate encoding of scalar complex fields," J. Opt. Soc. Am. A **24**, 3500–3507 (2007).

[25] J. P B. Mueller, N. A Rubin, R. C Devlin, B. Groever, and F. Capasso, "Metasurface polarization optics: independent phase control of arbitrary orthogonal states of polarization," Phys. Rev. Lett. **118**, 113901 (2017).

[26] G. Lee, J. Hong, S. Hwang, S. Moon, H. Kang, S. Jeon, H. Kim, J. Jeong, and B. Lee, "Metasurface eyepiece for augmented reality," Nat. Comm. **9**, 4562 (2018).

[27] R. C. Devlin, M. Khorasaninejad, W. T. Chen, J. Oh, and F. Capasso, "Broadband high-efficiency dielectric metasurfaces for the visible spectrum," Proc. Natl. Acad. Sci. **113**, 10473–10478 (2016).

[28] S. W. Daniel Lim, J. Park, D. Kazakov, C. M Spägele, A. H Dorrah, M. L Meretska, and F. Capasso, "Point singularity array with metasurfaces," Nat. Commun. **14**, 3237 (2023).

[29] C. Guo, M. Xiao, Y. Guo, L. Yuan, and S. Fan, "Meron spin textures in momentum space," Phys. Rev. Lett. **124**, 106103 (2020).

[30] C. Guo, M. Xiao, M. Orenstein, and S. Fan, "Structured 3D linear space–time light bullets by nonlocal nanophotonics," Light Sci. & Appl. **10**, 160 (2021).

[31] A. McWilliam, C. M Cisowski, Z. Ye, F. C Speirits, J. B Götte, S. M Barnett, and S. Franke-Arnold, "Topological approach of characterizing optical skyrmions and multi-skyrmions," Las. & Photon. Rev. **17**, 2300155 (2023).

[32] H. E. Kondakci and A. F. Abouraddy, "Optical space-time wave packets of arbitrary group velocity in free space," Nat. Commun. **10**, 929 (2019).

[33] M. Yessenov, Z. Chen, M. P. J. Lavery, and A. F. Abouraddy, "Vector space-time wave packets," Opt. Lett. **47**, 4131–4134 (2022).